Stop-flow lithography in a microfluidic device†

Dhananjay Dendukuri, Shelley S. Gu, Daniel C. Pregibon, T. Alan Hatton and Patrick S. Doyle*

Received 13th March 2007, Accepted 1st May 2007
First published as an Advance Article on the web 21st May 2007
DOI: 10.1039/b703457a

Polymeric particles in custom designed geometries and with tunable chemical anisotropy are expected to enable a variety of new technologies in diverse areas such as photonics, diagnostics and functional materials. We present a simple, high throughput and high resolution microfluidic method to synthesize such polymeric particles. Building off earlier work that we have done on continuous flow lithography (CFL) (D. Dendukuri, D. C. Pregibon, J. Collins, T. A. Hatton, P. S. Doyle, *Nat. Mater*., 2006, **5**, 365–369; ref. 1), we have devised and implemented a new setup that uses compressed air driven flows in preference to syringe pumps to synthesize particles using a technique that we call stop-flow lithography (SFL). A flowing stream of oligomer is stopped before polymerizing an array of particles into it, providing for much improved resolution over particles synthesized in flow. The formed particles are then flushed out at high flow rates before the cycle of stop-polymerize-flow is repeated. The high flow rates enable orders-of-magnitude improvements in particle throughput over CFL. However, the deformation of the PDMS elastomer due to the imposed pressure restricts how quickly the flow can be stopped before each polymerization event. We have developed a simple model that captures the dependence of the time required to stop the flow on geometric parameters such as the height, length and width of the microchannel, as well as on the externally imposed pressure. Further, we show that SFL proves to be superior to CFL even for the synthesis of chemically anisotropic particles with sharp interfaces between distinct sections.

1 Introduction

Polymeric microparticles and colloids are finding ever increasing use. The demand for such particles stems both from traditional applications[2] such as paints, coatings and column packings to more recent applications in optical devices,[3] drug delivery[4] and diagnostics.[5] While spherical particles are widely used, particles with exotic non-spherical shapes and chemical anisotropy are expected to help enable a range of exciting new technologies from photonic crystals[3] to multiplexed diagnostics.[5,6] However, there is no easy route to the synthesis of such particles. Emulsion and suspension polymerization based approaches that are widely used for the synthesis of polymeric particles do not offer the control of morphology and anisotropy that is essential for specialized particles. The ideal process for the synthesis of such complex particles should produce large numbers of monodisperse particles in custom designed shapes with the ability to fine tune chemical anisotropy as required. Additionally, the process should afford the use of materials that are functionalizable and biocompatible when required.

In the past few years, several microfluidic approaches to particle synthesis have been reported in the literature.[7] Most of these have been based on two-phase flow methods that lead to the formation of monodisperse droplets in microfluidic devices.[8–12] Large numbers of extremely monodisperse droplets of a desired polymer precursor are first produced using either a T-junction[8,9] or flow-focusing[10] geometries in a microfluidic device. The droplets are then polymerized using light or thermal polymerization to form monodisperse solid polymeric particles.[13,14] By confining droplets using the geometries of a microfluidic device and by using coflowing laminar streams, polymeric plugs and disks,[15,16] hemispheres,[17] core–shell particles[17] and Janus particles[18,19] were also created. However, these processes are still not very general in the morphologies that they can produce, being restricted to producing shapes that are either spherical or deformations of spheres.

Photolithography offers a much more general route to the synthesis of non-spherical particles because of the ability to use photomasks to precisely define shape. However, photolithography has not been used in particle synthesis applications because of the essential batch nature of the process which leads to low particle throughput. In addition, photoresist materials that are used in photolithography are not ideal for applications where biocompatibility or functionalization of the particles is essential. Further, creating chemically anisotropic particles using photolithography requires cumbersome multi-step alignment and protection techniques that are difficult to perform controllably and in a high-throughput fashion.

Recently, we combined the distinct advantages of microfluidics and projection-photolithography to propose a new method to synthesize polymeric particles called continuous flow lithography (CFL).[1] By taking advantage of the higher resolution synthesis and precise shape control intrinsic to photolithography along with the continuous processing

Department of Chemical Engineering, MIT 66-270, 77 Massachusetts Ave., Cambridge, MA 02139, USA. E-mail: pdoyle@mit.edu
† Electronic supplementary information (ESI) available: Movie showing the formation of particles in real-time. See DOI: 10.1039/b703457a

capabilities and laminar co-flow properties seen in microfluidic devices, we were able to successfully synthesize large numbers of monodisperse particles bearing complex shapes and tunable chemical anisotropy. In its simplest form, the process requires the use of only one phase, dispensing with the challenge of optimizing device surface chemistry in two-phase flows. Further, by using polymeric precursors with varying chemical properties, we were able to conveniently functionalize distinct sections of our particles with different chemical properties.[5,20]

In CFL, shuttered pulses (30–100 ms) of mask-defined UV light are flashed into a stream of oligomer flowing through a PDMS microchannel. The exposed portions of the oligomer are crosslinked by exposure to this light, leading to the formation of solid structures almost instantaneously. The structures formed are then able to advect through the continuously flowing polymer precursor liquid that surrounds them. This is because of the oxygen-induced inhibition[21] of polymerization at PDMS surfaces. During the polymerization process, oxygen diffuses in through the porous PDMS walls and reacts with free radicals, converting them to chain-terminating peroxide species. This results in the formation of a thin, uncrosslinked lubricating layer of oligomer near the PDMS walls that enables the particles to flow without sticking to the walls of the device.

However, because particles are synthesized in flow and exposed to finite pulses of UV light, they are smeared when high oligomer flow rates are used. In order to achieve a given particle resolution, there is therefore a limit to the maximum flow rate that can be used. This imposes restrictions on the particle throughput that can be achieved, a problem that is accentuated as particle size is decreased. There is a great need for the synthesis of complex particles at the colloidal length scale for applications such as drug delivery[4] or to achieve self-assembly by exploiting thermal forces.[22] With CFL, it is difficult to form such particles and throughput is a concern even for larger particles. The limitations of CFL arise from the fluidics and not the optics. Using i-line (365 nm) photolithography, features down to 400 nm can be achieved[23] provided high-quality photomasks and a stationery, non-flowing substrate are available.

In this article, we describe how we have overcome some of the above problems to form high resolution particles in a high throughput manner using a technique we call stop-flow lithography (SFL). Particles are formed in a stationery layer of monomer sandwiched inside a PDMS microchannel before being flushed out, the process being repeated in a cyclical manner. In order to perform SFL, it is vital to have a microfluidic system that responds rapidly to changes in pressure in order to switch frequently between stop and flow mode. We have devised a setup that uses compressed-air driven flows in preference to syringe pumps because of their improved dynamic response. However, the flow still takes a finite time to stop and start because of the deformation of the PDMS elastomer due to the imposed pressure. The deformation of PDMS has previously been exploited to design pressure-actuated valves,[24] peristaltic pumps[25] and pressure sensors[26] among other applications. However, in several other situations, the deformation of PDMS may be undesirable, causing sagging of channels,[27] increasing Taylor dispersion or simply diverging from predictions on flow profiles and mass transfer that have been made for rectangular cross-sections. Being the material of choice for numerous microfluidic applications, it is essential to characterize the effect of the deformation of PDMS on flow properties within microchannels.

The altered flow profile created at steady state by the bulging cross-section of rectangular PDMS devices has been studied in detail.[28] However, the dynamic response of the PDMS to an imposed pressure profile and its dependence on channel geometry and the imposed pressure are yet to be investigated. This dynamic response is of crucial importance in applications where the flow must be stopped and started frequently while also being important to predict when steady state will be achieved in continuous flow applications. In addition to describing the setup that we have devised to perform SFL, we have developed scaling relations to describe the effect of channel geometry on the dynamic response of the PDMS to changes in external pressure. Along with improved resolution, we show that operating the process in a stop-flow mode has the further advantage of increased throughput over CFL. Finally, we describe how SFL is superior to CFL when forming multifunctional particles with sharp interfaces.

2 Theory

The model described in this section involves a coupling between the fluid mechanics of oligomer flow and the elasticity of the PDMS device used. We start with a description of the channel geometry and then proceed to separately model the deformation of the PDMS microchannel and the lubrication flow created by the oligomer flowing through the PDMS device. The elasticity and flow problems are then coupled to provide a description of the squeeze flow that determines how rapidly the PDMS responds to changes in external pressure.

2.1 Microchannel geometry

We use PDMS microchannels bearing rectangular cross-sections that are sealed to a glass slide spincoated with PDMS (Fig. 1). In such devices, the top wall is a deformable layer of PDMS (Young's modulus, $E \simeq 1$ MPa[28]) that is several millimeters thick. Since the bottom wall of the device is a very thin layer of PDMS that is attached to a rigid glass slide ($E = 62$ GPa), its deformation can be neglected when compared to the top wall.

2.2 Modeling elasticity of PDMS

We start by assuming that Hooke's law can be used to model the stress–strain relationship in PDMS giving $\varepsilon = \sigma/E$, where ε is the strain, σ is the stress and E is the Young's modulus of PDMS. The stress experienced by the PDMS is proportional to the applied external pressure. An appropriate length scale is required to calculate the strain. Because the PDMS device is several millimeters thick and the channel is only a few microns tall, the PDMS can be considered a semi-infinite medium where strain vanishes at large distances from the channel. In such cases, the appropriate length scale for the strain in the z-direction is given by the channel width, W, and not the thickness of the PDMS device or the channel height.[29] We

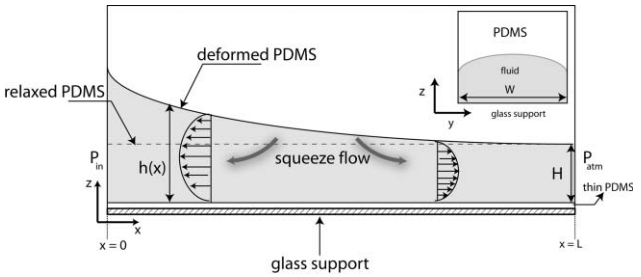

Fig. 1 Schematic showing the deformation of the PDMS microchannel (shown in white). The flow of the monomer (grey) is initially from left to right, the pressure being highest at the entrance and reaching atmospheric pressure at the outlet. The maximum PDMS deformation is thus at the leftmost point of the channel and the minimum deformation is at the rightmost point. The figure is a 2-dimensional representation of the channel where the height shown at any point, $h(x)$, has been averaged across the width of the channel (the y-dimension). The variation in height across the width is seen in a cross-sectional view of the channel that is shown in the inset on the top right of the figure. The deformed PDMS channel relaxes back to its original state, shown as a dashed line, when the pressure is turned off. This relaxation causes an asymmetric squeeze flow that drives monomer out to the left and the right. The bottom of the device is undeformed because of the rigid glass slide that supports it.

therefore have the deformation of the channel ceiling, Δh, being proportional to the channel width, local pressure and Young's modulus as given by

$$\varepsilon \sim \frac{\Delta h}{W} \sim \frac{P}{E} \tag{1}$$

As discussed in earlier work,[28] the deformation of the PDMS channel in the lateral direction (y-direction) can be neglected because it is in turn proportional to the height, H, which is much smaller than the width ($W/H \gg 1$) in all the experiments presented here.

The deformation in the height of the channel at any point is proportional to the local pressure according to eqn (1). Since the pressure decreases along the length of the channel, there is a commensurate decrease in PDMS deformation along the length of the device. The maximum deformation is observed at the entrance to the channel and is given by

$$\Delta h_{\max} \sim \frac{PW}{E} \tag{2}$$

2.3 Modeling fluid flow

The three-dimensional problem of fluid flow through a rectangular cross-section can be reduced to two dimensions by averaging the height of the deformed PDMS channel, $h(x,y)$, across the width of the channel at any cross-sectional interface along the length of the device to get $h(x)$ alone as shown in Fig. 1. For the creeping flow ($Re \ll 1$) of fluid through a thin channel ($H/L \ll 1$), the flow is mainly in the x-direction and the lubrication approximation can then be used to reduce the Navier–Stokes equation to,

$$\frac{\partial P}{\partial x} = \mu \frac{\partial^2 v_x}{\partial z^2} \tag{3}$$

Here μ is the viscosity of the oligomer. No-slip boundary conditions are imposed at the top and bottom walls. The continuity equation couples v_x and v_z, enabling us to calculate v_z.

$$\frac{\partial v_x}{\partial x} + \frac{\partial v_z}{\partial z} = 0 \tag{4}$$

The boundary conditions for v_z are dictated by the rigid bottom wall and the flexible top wall.

$$v_z(z = 0) = 0 \tag{5}$$

$$v_z(z = h(x)) = -\frac{\partial h}{\partial t} \tag{6}$$

Here, we have assumed that the curvature of the PDMS top wall is small in relation to the length of the device ($\Delta h_{\max}/L \ll 1$) from which it follows that the velocity of the retracting membrane is only in the negative z-direction. Integrating eqn (3) and using the associated boundary conditions, we get

$$v_x = \frac{1}{2\mu}\frac{\partial P}{\partial x}\left[z^2 - zh(x)\right] \tag{7}$$

2.4 Coupling of elasticity and flow

When an external pressure is first imposed, the rectangular cross-section of the PDMS device bulges as shown in the inset of Fig. 1. When the pressure is turned off, the elasticity of the PDMS forces the microchannel to retract back to its original rectangular cross-section, setting up a squeeze flow that drives excess fluid out of the device. The squeeze flow is asymmetric, driving more fluid towards the entrance of the channel than out through the exit. The flow continues until all the excess fluid is driven out and therefore has a characteristic timescale, τ_r, associated with it. In this work, we are concerned with how τ_r is affected by the material properties of the PDMS and the oligomer, channel geometry and the imposed pressure.

In elastohydrodynamic problems such as this one, the deformed PDMS exerts a pressure on the fluid confined within the channel.[30] For small deformations, the pressure exerted on the fluid at any point along the channel can be assumed to be proportional to the strain in the PDMS at that point as given by eqn (1). The appropriate length scale for the strain is again the width, W. The pressure at any point, x, is then given by

$$P(x) = E\frac{\Delta h(x)}{W} = E\left(\frac{h(x) - H}{W}\right) \tag{8}$$

where H is the undeformed height of the channel. Differentiating eqn (8), we get

$$\frac{\partial P}{\partial x} = \frac{E}{W}\frac{\partial h}{\partial x} \tag{9}$$

Using eqns (7) and (9), we now have

$$v_x = \frac{E}{2\mu W}\frac{\partial h}{\partial x}\left(z^2 - zh(x)\right) \tag{10}$$

Using eqn (4) to evaluate v_z, we get

$$v_z = -\int_0^z \frac{\partial v_x}{\partial x} dz \tag{11}$$

Using eqns (10) and (11), we can now evaluate v_z at $z = h(x)$ and equate it to the instantaneous velocity of the deforming membrane using eqn (6) to get

$$\frac{\partial h}{\partial t} = -\frac{h^2 E}{4\mu W}\left[\left(\frac{\partial h}{\partial x}\right)^2 + \frac{h}{3}\frac{\partial^2 h}{\partial x^2}\right] \tag{12}$$

We thus have a differential equation that describes $h(x,t)$. While a full solution to eqn (12) can be obtained only using numerical techniques, a simple scaling analysis reveals some insights into the problem. In the analysis that follows, we assume that channel deformation is small in comparison with channel height ($H \gg PW/E$). We first note that the scales for the height of the channel, $h(\sim H)$, and the deformation of the channel, $\Delta h(\sim PW/E)$, differ from each other. The scales for the other variables are $x(\sim L)$ and $t(\sim \tau_r)$ where the response time, τ_r, remains to be determined. For each of the three partial derivatives in eqn (12) we then obtain the following scalings

$$\frac{\partial h}{\partial t} \sim \frac{PW}{E\tau_r} \tag{13}$$

$$\left(\frac{\partial h}{\partial x}\right)^2 \sim \left(\frac{PW}{EL}\right)^2 \tag{14}$$

$$h\left(\frac{\partial^2 h}{\partial x^2}\right) \sim H\frac{PW}{EL^2} \tag{15}$$

Substituting these scalings into eqn (12) we get

$$\frac{1}{\tau_r} \sim \frac{H^2 E}{4\mu W L^2}\left[\frac{PW}{E} + \frac{H}{3}\right] \tag{16}$$

The first term inside the brackets on the right-hand side of eqn (16) can be neglected provided $H \gg PW/E$, which is exactly what we had assumed at the outset. Under these conditions we see that

$$\tau_r \sim \frac{\mu L^2 W}{EH^3} \tag{17}$$

We note from eqn (17) that the response time is then independent of the imposed pressure. When the pressure is increased to a point that the deformation in channel height, Δh, is comparable to the channel height, H, the scaling for the response time is more complicated because both terms inside the bracket in eqn (16) must then be taken into account.

3 Experiment

3.1 Microfluidic devices

Devices were fabricated by pouring polydimethylsiloxane (PDMS, Sylgard 184, Dow Corning) on a silicon wafer containing positive-relief channels patterned in SU-8 photoresist (Microchem). The thickness of the PDMS devices was always maintained to be 5 mm or greater. For the work shown in Fig. 2–6, straight channels with a rectangular cross-section and variable widths, lengths and heights were used as required. For Fig. 7, trident-shaped rectangular channels that were 300 μm in width and 40 μm in height were used.

Devices were fabricated by cutting out the PDMS channel using a scalpel, punching a hole at one end to make an inlet for the entering fluid and carving out a reservoir at the other end to collect the particles. The PDMS devices were then plasma sealed to glass slides spin-coated with PDMS after placing thin sacrificial layers of PDMS on the channel alone and on the region of the glass slide which sits right under the channel. This is to ensure that the oligomer was exposed only to non-plasma treated PDMS surfaces while ensuring that the device is still effectively sealed. Devices were mounted on an inverted microscope (Axiovert 200, Zeiss) and the formation of the microparticles was visualized using a CCD camera (KP-M1A, Hitachi). Video recordings of bead flow and particle formation were recorded at 30 frames s^{-1} onto a video tape recorder (DSR-25, Sony) for processing. Still images were captured and processed using NIH Image software or a digital camera (D200, Nikon) and Nikon Capture software.

3.2 Materials

In all experiments, the oligomer used was poly(ethylene glycol) (400) diacrylate (PEG-DA, Sigma Aldrich). For the experiments in Fig. 3 and 4, a 1% solution of 1.57 μm PMMA beads in PEG-DA was used. For the experiments in Fig. 5 and 6, the polymer precursor mix used was a 1% (w/v) solutions of the photoinitiator phosphine oxide phenyl bis(2,4,6-trimethyl benzoyl) (Irgacure 819, Sigma Aldrich) in PEG-DA. For the experiments in Fig. 7, a 0.005 wt% solution of the fluorescent monomer methacryloxy ethylthiocarbamoyl rhodamine B (Polysciences) in PEG-DA was used as the fluorescent stream. PEG-DA is reported by the manufacturer to have a viscosity of 56 cP at 25 °C.

3.3 Stop-flow-lithography setup

The setup for SFL requires the use of pressure provided by a compressed-air source to drive flow inside the microfluidic channels (Fig. 2). To generate controlled pressure in the range of 0–15 psi, a compressed air source (~40 psi) in the laboratory was first connected to either a T3510 I/P transducer (Marshbellofram) or a Type 100 LR manual pressure regulator (Control Air). Downstream of the transducer/regulator, a 3-way solenoid valve (Burkert) was used to switch rapidly between atmospheric pressure (stop) and the input pressure (flow). The output from the 3-way valve was connected to the microfluidic device using Tygon tubing connected to a 10 μl pipette tip (Biosciences). The pipette tip was filled with the desired fluid and inserted into the inlet hole punched in the microfluidic device. The transducer, 3-way valve and shutter were all controlled using VIs written in Labview 8.1 (National Instruments). The 3-way valve was controlled using a 1024-HLS digital I/O board (Measurement Computing) and a relay. The transducer and the shutter were controlled using serial

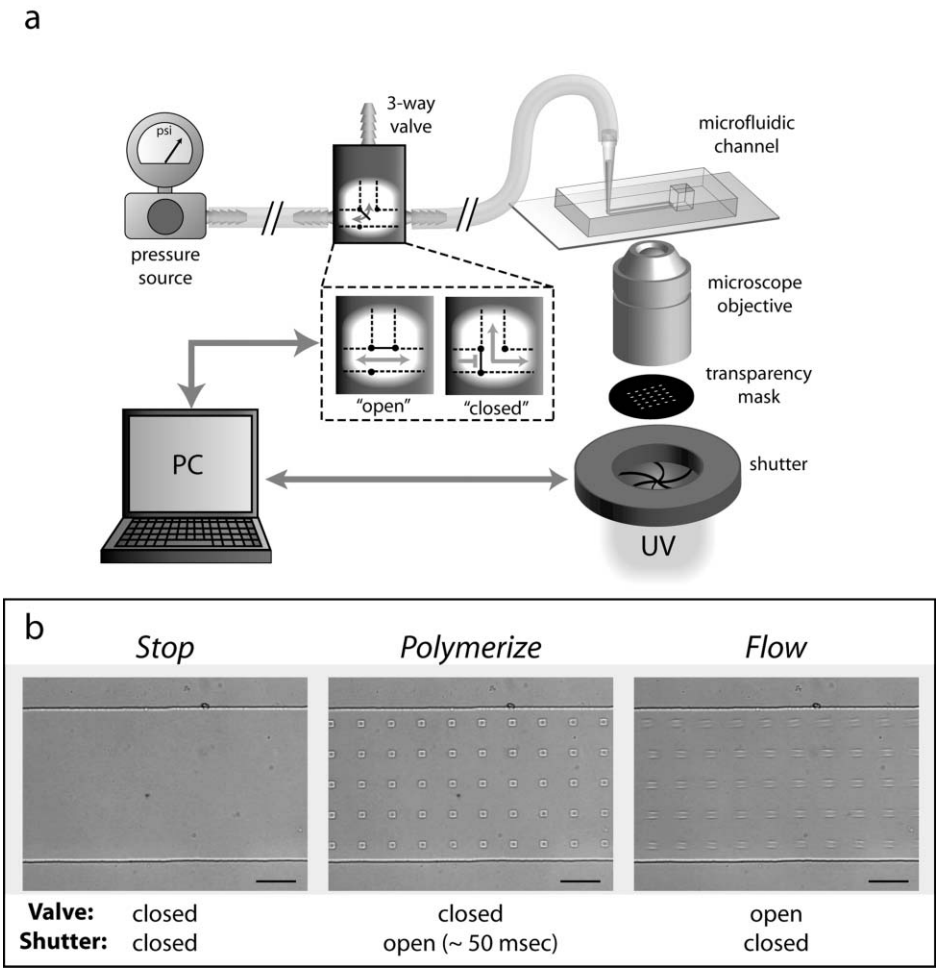

Fig. 2 Stop-flow lithography setup. (a) Schematic showing the computer-controlled flow setup. Oligomer flows within a microfluidic channel are driven using a pressure profile provided by a computer controlled 3-way solenoid valve that alternates between atmospheric pressure (closed) and a specified input pressure (open). The computer also controls the exposure time provided by the shutter. (b) Microscope images showing the three states of the process. In the first state (stop), the flow is stopped by closing the 3-way valve. In the second state (polymerize), an array of particles is polymerized into the stationery monomer film by opening the shutter for 0.05 s while keeping the 3-way valve closed. In the third state (flow), polymerized particles are flushed out of the channel by opening the 3-way valve while keeping the shutter closed. The scalebars shown in (b) are 50 μm.

connections. A movie showing the formation of particles in real-time is shown in the ESI (Movie1.mpg).† The experiment shown was performed using a channel of width 200 μm, height 20 μm and length 1 cm. The input pressure was 6 psi, t_{stop} = 0.3 s, $t_{polymerize}$ = 0.1 s and t_{flow} = 0.2 s.

3.4 Bead tracking

A dilute solution of PMMA beads in PEG-DA (see Materials section) was used to track the squeeze flow. After a given pressure profile was supplied, beads in the mid-plane of the channel ($z = H/2$ in Fig. 1) were followed with a 20× or 40× microscope objective (Zeiss) with an optivar setting of 2.5× leading to effective magnifications of 50× or 100× respectively. Movies of translating beads were recorded on to a video tape recorder (DSR-25, Sony) using a CCD camera that captured images at the rate of 30 frames s^{-1} using an exposure time of 1/500 s. The frame-to-frame position of beads was measured as they moved across the screen using macros written in NIH Image. Bead velocities were calculated from the displacement of the beads using the central difference approximation. Bead tracking was always performed at the exit of the channel to ensure consistency in experiments. Beads that were close to the center of the channel ($y = W/2$ in Fig. 1) were chosen to avoid wall effects.

3.5 Photopolymerization setup

Photomasks were designed in AUTOCAD 2005 and printed using a high resolution printer at CAD Art Services (Bandon, OR). Each mask was inserted into the field-stop of the microscope to be used for projection photolithography. A 100 W HBO mercury lamp served as the source of UV light. A filter set that provides wide UV excitation (11000v2: UV, Chroma) was used to select light of the desired wavelength and a VS25 shutter system (Uniblitz) driven by a computer controlled VMM-D1 shutter driver provided specified pulses of UV light. Typical exposure times used were 30–100 ms and pressures

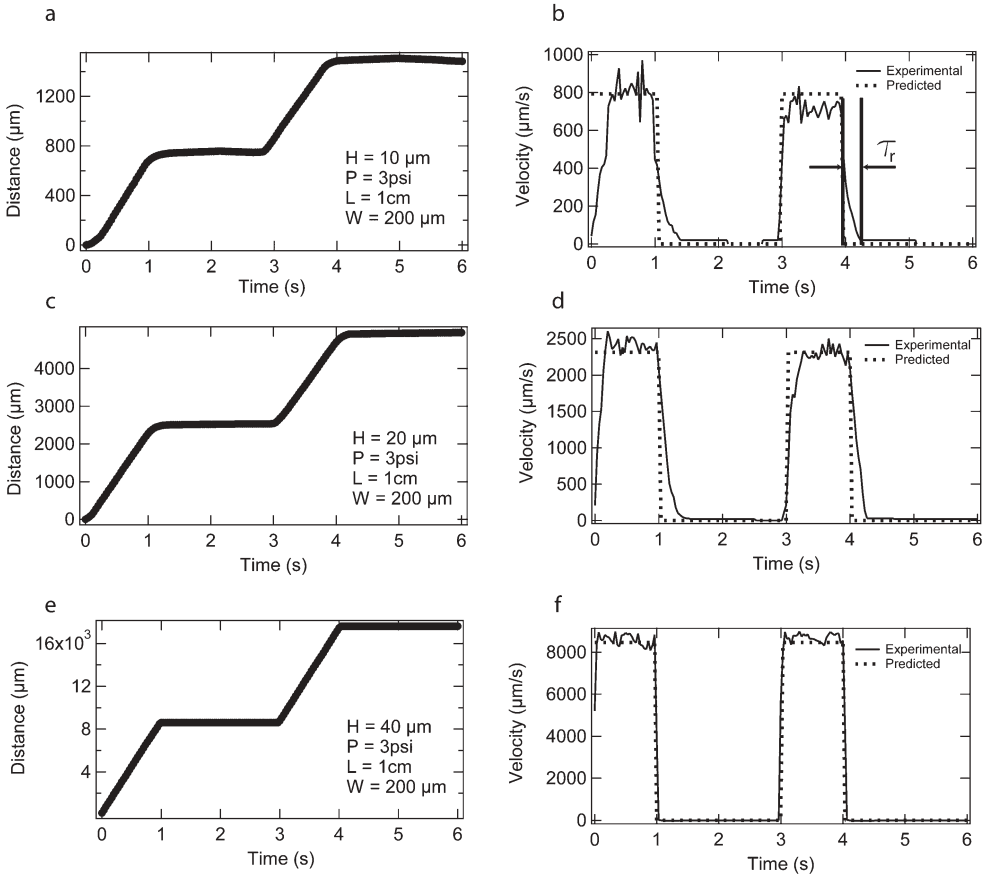

Fig. 3 Tracking of an individual bead in SFL. (a), (c) and (e) Plots showing the position in time of a 1.57 μm bead, subjected to a pulsed on–off pressure input profile that is on for a period of 1 s and off for a period of 2 s. The input pressure is 3 psi and the channels used are 200 μm wide and 1 cm long. The three plots, (a), (c) and (e) are for channels of heights 10, 20 and 40 μm respectively. (b), (d) and (f) Plots showing the velocity of the beads in (a), (c) and (e) calculated using the central difference method. The dotted lines represent the velocity that is predicted by eqn (18). As shown in (a), a finite response time is required for the velocity to reach its maximum value in each cycle and to decay from the maximum down to zero. We measure the response time (τ_r) as the time required for the velocity to drop to 1% of its maximum value as shown in (b).

ranged from 0.05 to 15 psi. A reservoir was cut in the PDMS to collect the particles.

4 Results

In microfluidic devices, fluid flows are commonly driven using syringe pumps. In displacement-driven flows such as these, the compression of the fluid in the tubing external to the microfluidic device causes transients that can be several minutes or longer for micron-scale systems.[31] Due to this effect, compressed air driven flows are preferable in applications where a rapid dynamic response is desired.[31,32] While they eliminate transients that are associated with the compression of fluid in the tubing outside the microfluidic device, air-driven flows still lead to finite transients associated with the deformation of the PDMS device.

In SFL (Fig. 2), three distinct steps—stop, polymerize and flow—are repeated in a cyclical fashion. In the first step, the pressure-driven oligomer flow through the device is stopped by switching from a specified input pressure to atmospheric pressure using the 3-way solenoid valve. The flow takes a finite time to stop as the PDMS retracts from its bulged state back to its rectangular cross-section (Fig. 1), squeezing fluid out of the device. In the second step, an array of particles is polymerized into the stationary oligomer using UV light by opening the shutter briefly (0.03–0.1 s). In the third step, the particle array is flowed out by switching the 3-way valve back from atmospheric pressure to the specified input pressure. The three variables to be specified then are the time required to stop the flow ($t_{stop} > \tau_r$), the time required to polymerize particles ($t_{shutter}$) and the time required to flush the particles out (t_{flow}). While $t_{shutter}$ and t_{flow} are easily determined, t_{stop} can be determined only after first estimating τ_r which serves as a lower bound for t_{stop}. We used bead tracking experiments to estimate τ_r as a function of the input pressure and channel geometry. Typical bead tracking experiments that were performed in 10, 20 and 40 μm tall channels are shown in Fig. 3. A repeating square wave pressure profile comprising two parts—1 s of flow and 2 s of stoppage—was applied to the system. In Fig. 3a, c and e, we show the position in time of a bead close to the exit of the channel. The bead is shown going through two cycles of stop and flow. The velocity of the bead is the derivative of its position and is shown in Fig. 3b, d and f. Also shown in the dotted lines are the predicted

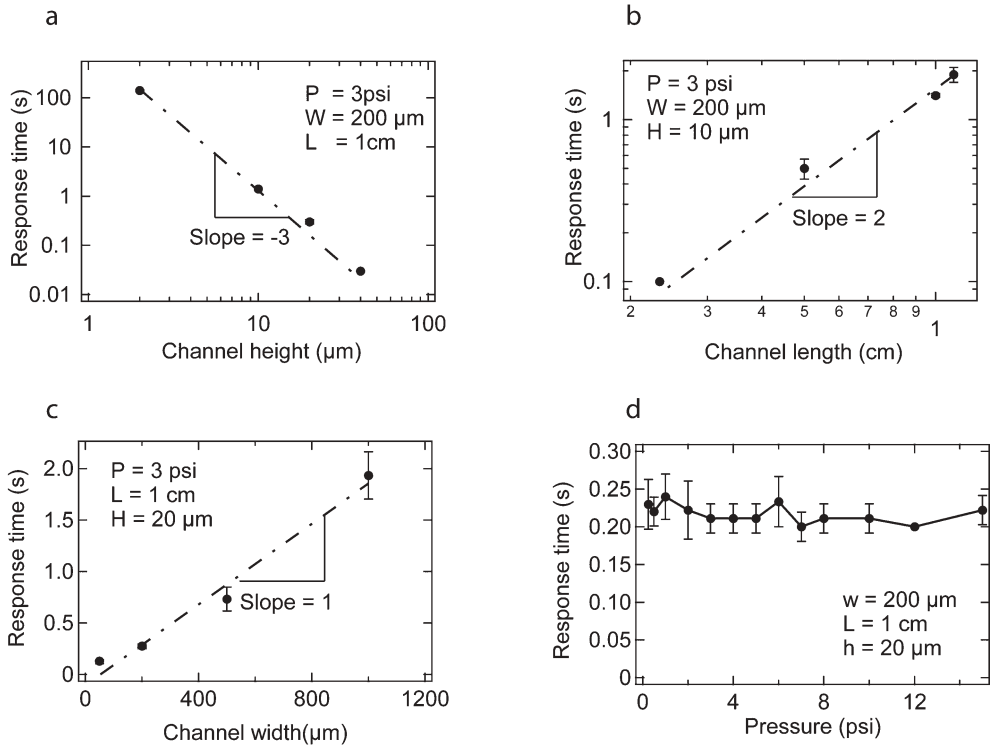

Fig. 4 Plots showing the dependence of τ_r on (a) channel height; (b) channel length; (c) channel width; and (d) pressure gradient. Dashed lines in a–c show the power law predicted by eqn (17). Our scaling theory predicts that τ_r is invariant with change in pressure.

maximum velocity, $U(L)$, that one would expect at the exit of a deforming PDMS channel,[28]

$$U(L) = \frac{3H^3E}{96W\mu L}\left[\left(1+\frac{PW}{EH}\right)^4 - 1\right] \qquad (18)$$

A finite response time is required for the bead velocity to attain a steady value after the imposition of an external pressure and for it to drop to zero after the pressure input has been turned off. This finite response is characterized by the curvature of the bead–displacement plots at the junction between the flat and sloped lines in Fig. 3a, c and e. The finite response can be seen more clearly in Fig. 3b, d and f by measuring the time required for the flow velocity to attain a steady value after it has been turned on or by measuring the time required for the flow velocity to stop after the pressure input has been turned off. For the purpose of this work, response times, (τ_r), were calculated by measuring the time required for bead velocity to fall to 1% of its maximum value.

We first verified the dependence of τ_r on channel height by performing experiments in channels of four different heights 2, 10, 20 and 40 μm with constant width 200 μm and length 1 cm. All experiments were performed at an input pressure of 3 psi. τ_r was calculated for each channel and the results were plotted against channel height. As seen in Fig. 4a, a power law of -3 is drawn through the experimental data, indicating that the scaling argument in eqn (17) compares very well with experiment. As channel height decreases, the sluggishness of the system increases because of the increased resistance to flow that must be overcome to squeeze the fluid out of the channel.

To verify the dependence of response time on channel length, we performed experiments in four channels of length equal to 0.25, 0.5, 1 and 1.2 cm, constant width of 200 μm, constant height of 10 μm, all at a pressure of 3 psi. Again, τ_r was calculated for each channel and plotted against channel length. As seen in Fig. 4b, a power law of 2 is drawn through the experimental data indicating that the scaling argument in eqn (17) holds. The resistance to driving a flow also increases with channel length causing larger length channels to show increasing response times.

To verify the dependence of response time on channel width, we performed experiments in four channels of widths 50, 200, 500 and 1000 μm, constant length 1 cm and constant height 20 μm, all at a pressure of 3 psi. The response time is observed to increase linearly with channel width as predicted by eqn (17). As width increases, the same deformation produces smaller restoring pressures according to eqn (8), resulting in an increased response time.

We also experimentally measured the dependence of τ_r on input pressure as shown in Fig. 4d. We see that the response time is invariant to pressure, within the limits that we have tested (up to 15 psi). Larger pressures led to the PDMS-PDMS seal in the device breaking. As predicted by eqn (17), this invariance is expected as long as the channel deformation is much smaller than the height of the channel. For the channels used in this experiment (H = 20 μm, W = 200 μm), the pressure at which the channel deformation becomes comparable to channel height ($P \sim EH/W$) is approximately 15 psi.

Increasing pressures cause larger deformations in the channel walls, which in turn increase the elastic driving force

that pushes the PDMS back. This increased driving force is counteracted by the fact that a larger volume of fluid must now be driven out. This balance between elastic and viscous forces ensures that response time is independent of pressure for small deformations. Finally, we see that τ_r varies as μ/E. This implies that using less viscous oligomers or making the PDMS devices stiffer, using a higher proportion of curing agent to base for example, will result in smaller response times. In summary, tall channel heights, short channel lengths and channel widths and high pressures (within the limits of mechanical stability) are preferred to obtain rapid dynamic response for device operation in SFL.

5 Improved resolution compared to CFL

One of the disadvantages of performing photolithography in a flowing stream of monomer is that the structures formed are smeared due to the finite exposure time. For a given resolution, defined as the percent increase in length scale of a particle that can be tolerated, there is an upper limit to the flow velocity that can be used. Increasing the velocity above this limit leads to unacceptable smearing and deformation of the particles formed, while lowering the velocity leads to commensurate decreases in particle throughput. This maximum velocity also decreases with feature size, accentuating the problem of achieving high throughput in CFL.

SFL helps overcome these problems because the oligomer is exposed to light pulses only when it is stationery. To illustrate this advantage, we made particles using the same masks, exposure times (0.05 s) and channel heights (10 μm) in both CFL and SFL under conditions that yielded equal particle throughput for both processes (7–30 particles s^{-1} depending on the size of the feature size). A comparison of the particles made using SFL *versus* CFL is shown in Fig. 5. Shown in the inset of Fig. 5a, b and c on the right are the transparency masks used to make the particles.

Concentric square masks of different sizes, where the region between the inner and outer squares was transparent to light were used to make the particles. The dimension described by half the difference between the inner and the outer sides of the concentric squares were 50 μm, 20 μm and 10 μm for the three different particles synthesized. This dimension is referred to as the smallest feature in the particles formed. A 20× objective was used to synthesize all particles in this study leading to a reduction in mask size of ~7.8 times because of a 2.57× lens in the optical train of the microscope (20/2.57 ~ 7.8). The smallest features of the particles synthesized were 6 μm (= 50/7.8), 2.5 μm (= 20/7.8) and 1.25 μm (= 10/7.8) which are shown in Fig. 5d, f and h respectively. Readily available transparency masks can be printed down to resolutions of ~10 μm, where the loss of image quality is already apparent (inset of Fig. 5c). This imposes a practical limit on the resolution and the feature size of particles that can be made using cheaply available transparency masks in SFL. However, using chrome masks, one may be able to achieve sharp features down to 1 μm. One other factor that must be noted is that hydrogel materials like PEG-DA are not optimized for use as photoresists. This may impose limitations on the smallest feature size that can be synthesized. We believe that our ability to achieve sharper features is thus limited by the masks and materials we are using as opposed to a fundamental limitation in the process itself.

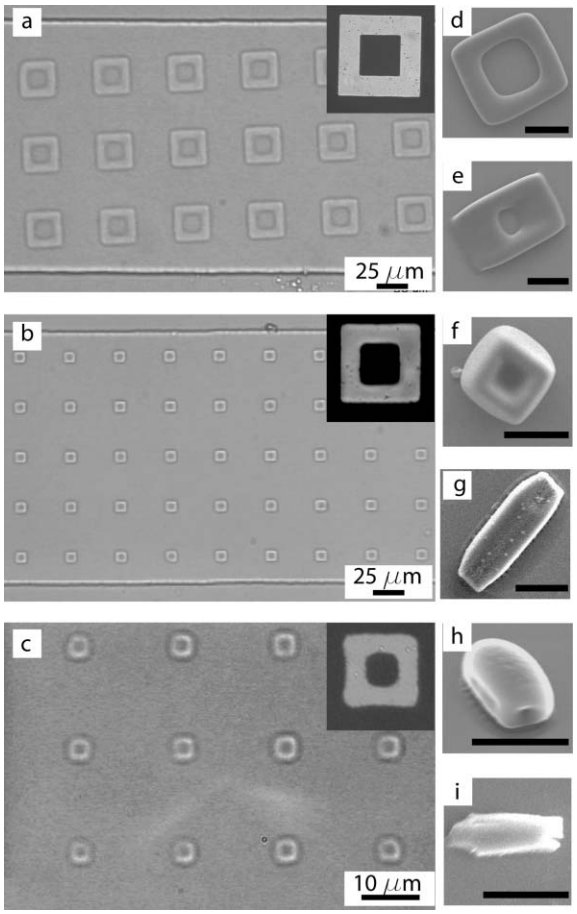

Fig. 5 Particles of three different feature sizes (see definition in text) formed using SFL. All particles were synthesized using a 20× microscope objective and a microchannel that was 200 μm wide, 10 μm tall and 1 cm long. In (a), (b) and (c) we show the synthesis, using SFL, of arrays of particles that have feature sizes of 6.25, 2.5 and 1.25 μm respectively. The inset on the top right of (a), (b) and (c) shows the transparency mask that was used to synthesize the particles. In (d), (f) and (h) are SEM images of particles in (a), (b) and (c) respectively. Particles with features down to a micron can be made using SFL. Note that the particles in (c) have a high aspect ratio so the particle in (h) is on its side. In (e), (g) and (i) we show SEM images of particles made with the same masks using CFL under conditions that yield identical throughput as SFL. The particles are smeared in comparison to the particles formed in SFL and are increasingly deformed as their size decreases. In (d)–(i) the scalebar is 10 μm.

As seen in Fig. 5, the particles formed using CFL are blurred beyond recognition even for the largest particles which have a feature size of 6 μm (Fig. 5e), while those formed using SFL show good resolution at 6 μm and 2.5 μm while the 1.25 μm feature (Fig. 5h) is visible but not sharp. Considerations of particle uniformity also make SFL more attractive than CFL. In CFL, the deformation of the channels during the formation of particles (Fig. 1) means that there may be some non-uniformity in the heights of the particles formed because the height of the channel varies with channel length when an external pressure is imposed.

6 Increased throughput

In addition to improved resolution, SFL also provides far greater throughput than CFL. After polymerizing an array of particles, one can flush the particles out at a high velocity, leading to a much greater average flow velocity than in CFL. The maximum throughput (particles s^{-1}) that can be achieved using SFL, T_s, is

$$T_s = \frac{N_p}{t_{stop} + t_{polymerize} + t_{flow}} = \frac{N_p}{\tau_r + \tau_{shutter} + L/v} \qquad (19)$$

where N_p is the maximum number of particles that can be polymerized in one exposure and is dependent on the spot size of the objective and the particle size, τ_r is the response time required for the flow to stop, $\tau_{shutter}$ is the time the shutter is left open to polymerize particles, L is the length of the channel full of particles that needs to be flushed out and v is the flow velocity used to flush out the particles. The spot size of the microscope objective used limits the number of particles that can be produced as $N_p \sim D_s^2$ where D_s is the diameter of the spot. For example, we are currently limited to producing approximately two thousand 10 μm particles per exposure (using a fractional area coverage of 0.2) using a 20× microscope objective that has a spot size one millimeter in diameter. Using the experimentally determined response times, τ_r, for different channel heights, a channel width of 1000 μm and a channel length of 1 cm, the maximum input pressure (P = 15 psi) that safely preserves the stability of seals in the all-PDMS device and an exposure time of 0.05 s, we obtained maximum values for T_s that are plotted in Fig. 6. As channel height decreases, τ_r increases and the velocity that can be achieved using the same pressure decreases, increasing the time required to flow out the particles. The maximum throughput achievable using SFL therefore decreases with a decrease in channel height. In comparison, the maximum throughput achievable using CFL, T_c, is given by

$$T_c = \frac{N_p}{t_{polymerize} + t_{flow}} = \frac{N_p}{\tau_{shutter} + L/v_{max}} \qquad (20)$$

where all the variables are as defined previously except v_{max} which is the maximum velocity that can be used without compromising on particle resolution and is a function of particle size. For simplicity, we have calculated v_{max} as that velocity which leads to 10% of smearing in the length of the particle parallel to the flow. T_c is also plotted in Fig. 6.

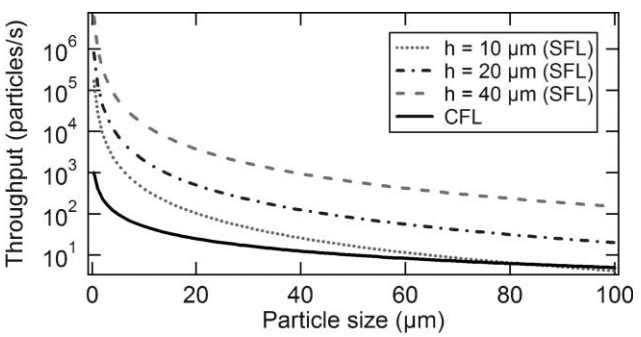

Fig. 6 Particle throughput (particles s^{-1}) as a function of particle size for both CFL and SFL. The curves have been plotted using eqns (19) and (20). As particle size decreases, SFL offers an increased advantage in throughput over CFL. As channel height increases, SFL throughput increases because of the reduced response time required for the PDMS to equilibrate.

As seen in Fig. 6, SFL can produce orders of magnitude more particles than CFL. The gap between the two processes also widens as particle size is decreased. This is because the maximum velocity that can be used to form particles decreases with size in CFL whereas in SFL, the maximum velocity that can be used is independent of particle size. For example, using only our current simple setup, SFL can produce 3 μm feature particles at the rate of 10^7 min^{-1} in a 40 μm tall channel. This high throughput is achieved by clocking as many as six stop-polymerize-flow cycles in one second. These numbers are much higher than other microfluidic techniques[15–17] that have recently been reported, all of which generate particles at the rate of 10^3–10^4 particles min^{-1}, while not affording the flexibility in particle shape that our process offers. Despite the small spot size of the microscope objective we are using, the throughput also compares well with particle technologies that make use of large area steppers conventionally used for photolithographic applications in the IC industry.[33] Such batch processes are limited to processing one 5″ wafer every minute which leads to a throughput of approximately 2.5 × 10^8 particles (~3 μm in size) min^{-1}. This does not include the time that is required to develop and extract the particles from each individual wafer. Because of the nature of our process, we can perform as many as 300 exposure cycles min^{-1} by rapidly cycling through the stages of stop-polymerize-flow. Particles are then flowed out into a large reservoir where they can be developed and collected in one step at the end. With access to a commercial stepper, we would then be able to achieve a throughput that was at least two orders of magnitude higher than these photolithographic batch processes. Further, our process is unique in allowing us to synthesize particles using materials that cannot be easily spin-coated, enabling the use of a much wider range of materials than traditional photolithographic techniques.

The ability to synthesize large numbers of monodisperse particles in a variety of shapes would help enable fundamental studies in rheology and self-assembly besides being important for the viability of nascent particle-based technologies.[5] The rheology of particle suspensions is very sensitive to particle shape[34] and important in the design of bullet resistant fabrics,[35] paints and consumer products. SFL can be used to produce model solutions of precisely defined particles which can be used to characterize the effect of particle shape on rheology. In self-assembly applications, SFL could be used to generate large numbers of complex particles that will serve as building blocks[22] to induce the assembly of larger structures through Brownian collisions.

7 Multi-functional particles with sharp interfaces

One of the unique advantages of flow lithography in microfluidic devices is the ability to exploit laminar flow to polymerize across multiple distinct streams, forming particles with multiple adjacent chemistries.[5,20] Such particles are finding use in several applications including multiplexed

detection[5] and self assembly.[20] When using miscible fluids, the diffusion of species between the streams can deplete the sharpness of the interfaces between adjacent chemistries[36]—an occurrence that is typically undesirable. We demonstrate how SFL can be used to minimize diffusion across streams, improving the sharpness of the interfaces between particle chemistries.

We made tri-functional, striped rods to investigate the interfaces between fluorescent and non-fluorescent particle chemistries when using CFL and SFL (Fig. 7). We used a channel with three inlets that were connected in parallel to the same pressure source: this eliminates lateral flow and maintains constant stream widths. As such, any 'smearing' of the interfaces between the particle chemistries is expected to result only from diffusion of the fluorescent species between streams.

We made particles that were $\sim$270 μm-wide, and 30 μm-deep using an exposure time of 50 ms in a 40 μm-tall channel approximately 200 μm after the stream junction (Fig. 7a). For particle synthesis using CFL, we chose a flow velocity of $\sim$50 μm s^{-1} to limit the expected distortion of the width (during polymerization) to $\sim$10% (50 m s^{-1} × 0.05 s = 2.5 μm) while for SFL, we used a much higher velocity of $\sim$1000 μm s^{-1} with a t_{stop} of 50 ms. Because of the small exposure times ($t_{polymerize}$ = 50 ms) used, the diffusion of the fluorescent species across the interface ($l = \sqrt{Dt_{polymerize}}$) between the streams is small ($\sim$2 μm) when compared to the length of the particle given that the diffusivity in such viscous materials is typically on the order of 10^{-10} m^2 s^{-1}.[37] This simple analysis does not take into account the instant viscosification of the oligomer during crosslinking that results in even lower diffusivities and sharper interfaces in practice.

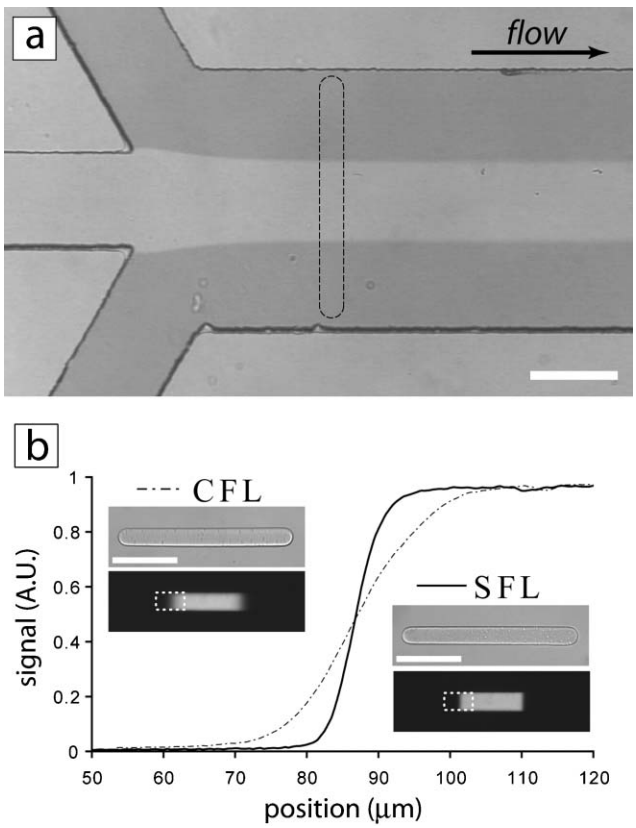

Fig. 7 Interface comparison of multi-functional particles made using CFL and SFL. (a) Striped, rod-shaped particles were formed by polymerizing for 0.05 s across three adjacent streams in a microfluidic channel (300 μm wide, 40 μm tall) with three inlets (center stream loaded with fluorescent dye) that were connected to a common pressure source to maintain constant stream widths. (b) A scan of fluorescent intensity along the particles at a fluorescent/non-fluorescent interface. The inset shows DIC and fluorescence images of particles made using CFL at a flow velocity of $\sim$50 μm s^{-1}, and SFL with a velocity of $\sim$1,000 μm s^{-1} with a t_{stop} of 0.05 s. Scalebars in (b) are 100 μm.

After particles were synthesized and rinsed, we took scans of fluorescent intensity along the length of the particles (and entire width) at the fluorescent/non-fluorescent interfaces (Fig. 7b). As can be seen, the particles made using SFL show a dramatically sharper interface than those using CFL because we were able to use a higher velocity. This difference would be even more dramatic if it was necessary to preserve smaller feature sizes, which would further decrease the velocity for CFL. Therefore, the benefit of using SFL for synthesis of multi-functional particles is threefold, improving (1) throughput, (2) resolution, and (3) sharpness of interfaces.

8 Conclusion

In this work, we have demonstrated that stop-flow lithography can be used as a high throughput method for the synthesis of polymeric particles and structures down to the colloidal length scale. Operating the process in stop-flow mode is preferable to the previously demonstrated continuous flow lithography (CFL) because both improved resolution and dramatically higher particle throughput are achieved. One of the attractive features of flow lithography is its ability to form free-standing structures in any free-radical polymer precursor material. This enables the fabrication of particles and structures in a diverse range of functionalizable polymers that are not accessible to traditional photolithographic techniques because they cannot be spin-coated. SFL represents an important step towards performing high resolution photolithography for the formation of non-spherical colloidal structures in a variety of materials. We have also shown in this paper that the synthesis of multifunctional particles with sharp interfaces between the distinct sections can be achieved much more easily using SFL than CFL.

There is further work to be undertaken in order to push the process towards better resolution and higher particle throughput. Sub-micron resolution can be achieved by pushing device height down to a few microns and/or using immersion objectives. Particle throughput is currently limited by the spot size of the microscope objectives that we are using. However, the setup can quite easily be extended to produce orders of magnitude more particles simply by using larger area exposure lamps and microchannels that span larger dimensions. We believe that SFL represents a considerable advance in making flow lithography amenable to the synthesis of a variety of polymeric particles in a simple yet high throughput fashion.

Acknowledgements

We gratefully acknowledge the support of NSF NIRT Grant No. CTS-0304128 for this project. This research was also supported in part by the U.S. Army through the Institute for Soldier Nanotechnologies, under Contract DAAD-19-02-D-0002 with the U.S. Army Research Office. The content does not necessarily reflect the position of the Government and no official endorsement should be inferred.

References

1 D. Dendukuri, D. C. Pregibon, J. Collins, T. A. Hatton and P. S. Doyle, *Nat. Mater.*, 2006, **5**, 365–369.
2 *Polymer Dispersions and Their Industrial Applications*, ed. D. Urban and K. Takamura, Wiley-VCH, Weinheim, Germany, 2002, pp. 15–39.
3 Y. Lu, Y. Yin and Y. Xia, *Adv. Mater.*, 2001, **13**, 415–420.
4 R. Langer and D. A. Tirrell, *Nature*, 2004, **428**, 487–492.
5 D. C. Pregibon, M. Toner and P. S. Doyle, *Science*, 2007, **315**, 1393–1396.
6 N. H. Finkel, X. Lou, C. Wang and L. He, *Anal. Chem.*, 2004, **76**, 352A–359A.
7 J. L. Steinbacher and D. T. McQuade, *J. Polym. Sci., Part A: Polym. Chem.*, 2006, **44**, 6505–6657.
8 T. Kawakatsu, Y. Kikuchi and M. Nakajima, *J. Am. Oil Chem. Soc.*, 1997, **74**, 317–321.
9 T. Thorsen, R. W. Roberts, F. H. Arnold and S. R. Quake, *Phys. Rev. Lett.*, 2001, **86**, 4163–4166.
10 S. L. Anna, N. Bontoux and H. A. Stone, *Appl. Phys. Lett.*, 2003, **82**, 364–366.
11 S. Okushima, T. Nisisako, T. Torii and T. Higuchi, *Langmuir*, 2004, **20**, 9905–9908.
12 A. S. Utada, E. Lorenceau, D. R. Link, P. D. Kaplan, H. A. Stone and D. A. Weitz, *Science*, **308**, 537–541.
13 S. Sugiura, M. Nakajima, J. Tong, H. Nabetani and M. Seki, *J. Colloid Interface Sci.*, 2000, **227**, 95–103.
14 T. Nisisako, T. Torii and T. Higuchi, *Chem. Eng. J.*, 2004, **101**, 23–29.
15 D. Dendukuri, K. Tsoi, T. A. Hatton and P. S. Doyle, *Langmuir*, 2005, **21**, 2113–2116.
16 S. Xu, Z. Nie, M. Seo, P. Lewis, E. Kumacheva, H. A. Stone, P. Garstecki, D. B. Weibel, I. Gitlin and G. M. Whitesides, *Angew. Chem., Int. Ed.*, 2005, **44**, 724–728.
17 Z. Nie, S. Xu, M. Seo, P. C. Lewis and E. Kumacheva, *J. Am. Chem. Soc.*, 2005, **127**, 8058–8063.
18 T. Nisisako, T. Torii, T. Takahashi and Y. Takizawa, *Adv. Mater.*, 2006, **18**, 1152–1156.
19 R. F. Shepherd, J. C. Conrad, S. K. Rhodes, D. R. Link, M. Marquez, D. A. Weitz and J. A. Lewis, *Langmuir*, 2006, **22**, 8618–8622.
20 D. Dendukuri, T. A. Hatton and P. S. Doyle, *Langmuir*, 2007, **23**, 4669–4674.
21 C. Decker and A. D. Jenkins, *Macromolecules*, 1985, **18**, 1241–1244.
22 S. C. Glotzer, *Science*, 2004, **306**, 419–420.
23 K. Nakagawa, M. Taguchi and T. Ema, *IEDM Tech. Dig.*, 1990, 817–820.
24 M. A. Unger, H.-P. Chou, T. Thorsen, A. Scherer and S. R. Quake, *Science*, 2000, **288**, 113–116.
25 A. Y. Fu, H.-P. Chou, C. Spence, F. H. Arnold and S. R. Quake, *Anal. Chem.*, 2002, **74**, 2451–2457.
26 K. Hosokawa, K. Hanada and R. Maeda, *J. Micromech. Microeng.*, 2002, **12**, 1–6.
27 E. Delamarche, H. Schmid, B. Michel and H. Biebuyck, *Adv. Mater.*, 1997, **9**, 741–746.
28 T. Gervais, J. El-Ali, A. Gunther and K. F. Jensen, *Lab Chip*, 2006, **6**, 500–507.
29 T. Gervais, PhD Thesis, Massachusetts Institute of Technology, 2005.
30 J. Skotheim and L. Mahadevan, *Phys. Rev. Lett.*, 2004, **92**, 245509.
31 H. A. Stone, A. D. Stroock and A. Ajdari, *Annu. Rev. Fluid Mech.*, 2004, **36**, 381–411.
32 C. Fütterer, N. Minc, V. Bormuth, J.-H. Codarbox, P. Laval, J. Rossier and J.-L. Viovy, *Lab Chip*, 2004, **4**, 351.
33 C. Hernandez and T. Mason, *J. Phys. Chem. C*, 2007, **111**, 4477–4480.
34 S. C. Tsai, D. Botts and J. Plouff, *J. Rheol.*, 1991, **36**, 1291–1305.
35 Y. S. Lee, E. D. Wetzel and N. J. Wagner, *J. Mater. Sci.*, 2003, **38**, 2825–2833.
36 R. Ismagilov, A. Stroock, P. Kenis, G. Whitesides and H. A. Stone, *Appl. Phys. Lett.*, 2000, **76**, 2376–2378.
37 J. Strauch, J. McDonald, B. E. Chapman, P. W. Kuchel, B. S. Hawkett, G. E. Roberts, M. P. Tonge and R. G. Gilbert, *J. Polym. Sci., Part A: Polym. Chem.*, 2003, **41**, 2491–2501.

